Spin-polarized scanning tunneling microscopy and spectroscopy of ferromagnetic Dy(0001)/W(110) films

L. Berbil-Bautista,* S. Krause, M. Bode,† and R. Wiesendanger
Institute of Applied Physics and Microstructure Research Center, University of Hamburg, Jungiusstrasse 11, 20355 Hamburg, Germany
(Received 13 February 2007; published 8 August 2007)

Spin-polarized scanning tunneling microscopy and spectroscopy (SP-STS) are employed to investigate the contrast mechanism and the magnetic structure of Dy films epitaxially grown on W(110). While relatively complicated tip preparation procedures were necessary in the past, we now obtain magnetic contrast by bringing the tip in gentle contact with a ferromagnetic Dy film. Maximum contrast is observed at bias voltages around −0.9 V. Since highly polarized sample states are not available at the corresponding binding energy, we suggest that an unoccupied tip state is responsible for the strong magnetic contrast. SP-STS measurements show three-, four-, or sixfold magnetic contrast. This result can be explained by random azimuthal orientations of the tip magnetization with respect to the sample's easy axis. Images of the magnetic domain structure show a stripe domain pattern which consists of about 40 nm wide domains, the magnetization directions of which alternate by 60°. This result is a clear proof that the Dy(0001) surface exhibits ferromagnetic order. The domain walls are identified as Néel walls with a width of 2–5 nm.

DOI: 10.1103/PhysRevB.76.064411 PACS number(s): 75.60.Ch, 68.37.Ef

I. INTRODUCTION

In rare-earth metals, the competition between indirect exchange coupling, magnetocrystalline anisotropy, and magnetoelastic interaction results in a rich variety of magnetic structures in single crystals[1–4] and multilayers.[5–9] Moreover, the presence of surfaces and interfaces may strongly modify the bulk magnetic structure of rare-earth metal films and multilayers. For example, an enhanced surface ferromagnetic order has been observed for helimagnetic holmium films.[10] A recent resonant soft x-ray scattering study performed by Ott *et al.* in Ref. 11 reveals a complex magnetic depth profile for the phase transition between helimagnetic and ferromagnetic Dy/W(110) films. Namely, their experiments suggest that within the surface sensitivity of resonant soft x-ray scattering, i.e., averaged over about the film's 20 AL (atomic layer) underneath the surface and/or vacuum interface, no ferromagnetic order exists. Instead, Ott *et al.*[11] propose a so-called near-surface helimagnetic phase which is characterized by a lower value of the helimagnetic angle than in the bulk. While the spatially averaged physical properties of extended samples have been investigated in numerous studies,[5,12] only little is known about their surface magnetic domain structure, mainly because the magnetic correlation length is expected to be very short and experimental methods with adequate spatial resolution were not available in the past.

During the recent two decades, however, spin-polarized scanning tunneling microscopy/spectroscopy (SP-STM/STS) emerged as a magnetic imaging technique with an unprecedented surface sensitivity and a lateral resolution down to the atomic scale.[13–15] The contrast mechanism bases on the tunneling magnetoresistance effect which is well known from planar junctions,[16,17] albeit the insulating barrier of planar junctions is replaced by a vacuum barrier.[18] Two magnetic electrodes are involved: the surface to be investigated and the tip. Past experiments were performed with tips which were fabricated either by etching and polishing of magnetic bulk material[19,20] or by coating a nonmagnetic tip with a ferro- or antiferromagnetic thin film.[21–23]

Here, we show that magnetic tips for SP-STM/STS experiments can also be obtained by bringing the tip in singular gentle contact with a ferromagnetic Dy film which presumably leads to the transfer of a small Dy cluster from the sample's surface onto the tip apex. After returning to normal STM operation parameters, such probe tips provide highest magnetic contrast at bias voltages of about $U=-0.9$ V, i.e., far away from the binding energy of the highly spin-polarized Dy surface state and any other sample-related bulk state. We suggest that the strong magnetic contrast is caused by a highly spin-polarized unoccupied electronic state of the Dy cluster. With such tips, we obtain either three-, four-, or sixfold magnetic contrast which can nicely be explained by random variations of azimuthal orientations of the tip magnetization with respect to the sample's easy axis. Images of the magnetic domain structure show a stripe domain pattern which consists of about 40 nm wide domains, the magnetization direction of which alternate by 60°. This result is a clear proof that the Dy(0001) surface exhibits ferromagnetic order, in contrast to the near-surface helimagnetic phase proposed in Ref. 11. The domain walls are identified as Néel walls with a width of 2–5 nm.

This paper is organized as follows: After a brief introduction into the experimental setup and the measurement procedures (Sec. II), we will briefly review the structural, electronic, and magnetic properties of bulk Dy and the Dy(0001) surface (Sec. III). The main results of spin-averaged and spin-resolved SP-STS will be presented in Sec. IV A and Sec. IV B, respectively. Spatially resolved data showing the domain and domain wall structure of Dy/W(110) are shown in Sec. IV C and the domain walls are analyzed in Sec. IV D.

II. EXPERIMENT

The SP-STM experiments were performed in an ultrahigh vacuum system with two separate chambers: a preparation

chamber for the tip and sample treatment and an analysis chamber for sample surface characterization by means of low-energy electron diffraction (LEED) and Auger-electron spectroscopy (AES). Furthermore, a satellite of the analysis chamber contains a homebuilt scanning tunneling microscope which operates at temperatures between 20 and 300 K. We would like to emphasize that within our experimental setup, not only the sample but the entire microscope including the tip is cooled. The base pressure in both chambers is in the low 10^{-11} torr range.

A. Tip preparation

We use polycrystalline W tips which are electrochemically etched *ex situ* and cleaned *in vacuo* by a high-temperature flash at $T \geqslant 2200$ K. Two different types of magnetic tips were used; antiferromagnetic Cr-coated W tips and Dy cluster tips. The preparation of Cr-coated tips is described in detail in Refs. 14 and 21. In this work, we mainly used tips with a relatively thick Cr coating layer of at least 100 AL. It is well known that these tips are preferentially magnetized perpendicular to the tip axis,[22,24] i.e., parallel to the sample's surface plane and exhibit no stray field. As an alternative method for obtaining magnetic contrast, flashed W tips were brought in gentle contact with a Dy film, i.e., by dipping the tip several nanometers into the film or by switching off the feedback loop for one scan line while scanning the Dy surface. Thereby, a Dy cluster is probably transferred from the sample to the tip upon contact. Our results indicate that such Dy cluster tips exhibit a strong and stable in-plane magnetic contrast, which may be caused by the shape anisotropy of the Dy film attached to the relatively flat apex of the flashed tip. Obviously, the Dy clusters are large enough to be ferromagnetic at the measurement temperature of 60 K. Otherwise, the (super)paramagnetic behavior of the clusters would result in vanishing or unstable contrast. Although the tip properties seem to be less controllable with the latter method, it has the advantage that it may be repeated as often as necessary until a satisfactory tip magnetization direction and polarization is obtained. By adding a modulation voltage $U_{\mathrm{mod}}=25\ \mathrm{mV_{rms}}$ to the sample bias U and by detecting the dI/dU signal by lock-in technique, maps of the spin-resolved differential tunneling conductance dI/dU (magnetic signal) were recorded simultaneously with the constant-current images (topography).

B. Magnetic contrast mechanism

The contrast mechanism of spin-polarized STM has been explained by Wortmann *et al.*[25] who generalized the Tersoff-Hamann tunneling theory.[26,27] According to this work, the spin-resolved differential tunneling conductance dI/dU can be expressed by the sum of a spin-averaged and a spin-polarized contribution, dI/dU_{SA} and dI/dU_{SP}, respectively:

$$\frac{dI}{dU}(\vec{r}_t,U) \propto \underbrace{n_t \cdot n_s(\vec{r}_t,eU)}_{dI/dU_{\mathrm{SA}}} + \underbrace{\vec{m}_t \cdot \vec{m}_s(\vec{r}_t,eU)}_{dI/dU_{\mathrm{SP}}}, \qquad (1)$$

where n_t and $\vec{m}_t$ are the spin-averaged and magnetic tip density of states at the Fermi level, and $n_s(\vec{r}_{t,eU})$ and $\vec{m}_s(\vec{r}_{t,eU})$ the respective sample properties at the tip position $\vec{r}_t$ and energy eU. In this framework, the differential conductance dI/dU can be decomposed in a spin-averaged part and a spin-dependent part, where the spin-dependent part is proportional to the projection of $\vec{m}_s$ onto $\vec{m}_t$.

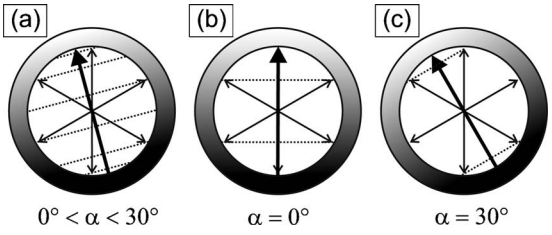

FIG. 1. Schematic representation of the possible orientations of the tip magnetization $\vec{m}_t$ (thick arrow) with respect to the six possible easy axis magnetization directions $\vec{m}_s$ of Dy (thin arrows): (a) $0° < \alpha < 30°$, (b) $\alpha = 30°$, and (c) $\alpha = 0°$, resulting in six, four, and three contrast levels, respectively. α denotes the azimuthal angle between $\vec{m}_t$ and $\vec{m}_s$ of the domain with the largest dI/dU signal.

According to Eq. (1), the magnetic contrast in dI/dU maps depends on the scalar product of $\vec{m}_t$ with $\vec{m}_s$, or—in other words—on the projection of $\vec{m}_s$ onto $\vec{m}_t$. In the case of an in-plane magnetic sample surface with six degenerate magnetization directions as expected for Dy(0001), this generally results in up to six dI/dU signal levels, as schematically represented in Fig. 1(a). We have to consider, however, that the azimuth of the tip magnetization cannot be controlled in our experiment and may accidentally coincide with high symmetry axes of the sample magnetization. For example, it may occur that the tip magnetization $\vec{m}_t$ lies along the sample's easy [Fig. 1(b)] or hard axis [Fig. 1(c)]. In these cases, the angle between $\vec{m}_t$ and $\vec{m}_s$ of the domain with the largest dI/dU signal is $\alpha = 0°$ or $\alpha = 30°$, respectively. As symbolized by hatched lines, this leads to a reduced number of contrast levels since in each case, magnetization directions can be found which are mirror symmetric with respect to $\vec{m}_t$ and therefore result in the same dI/dU signal. Namely, we expect four contrast levels if $\alpha = 0°$ and only three contrast levels if $\alpha = 30°$.

III. PROPERTIES OF Dy

A. Bulk properties

Dysprosium (Dy) is a rare-earth metal (REM) which crystallizes in the hcp structure. In the bulk, Dy exhibits two magnetic phase transitions: a second order phase transition from paramagnetic to helimagnetic at the Néel temperature $T_N = 178$ K and a first order phase transition from helimagnetic to ferromagnetic at the Curie temperature $T_C = 85$ K.[28,29] Below T_N, Dy exhibits ferromagnetic order within each individual basal (0001) plane but the magnetization rotates between adjacent planes thereby forming a helimagnetic structure. The angle between the magnetization in two subsequent basal planes varies between 43° at T_N and 26° at T_C.[29] Below T_C, the magnetization lies in the basal plane along the $\langle 2\bar{1}\bar{1}0 \rangle$ magnetic easy axes. Consequently,

six equivalent directions of magnetization are possible. The spin-resolved results presented in this work are taken at temperatures well below the bulk T_C.

B. Thin film growth

The preparation of clean lanthanide-metal surfaces from a bulk single crystal is almost impossible, not only due to their extreme reactivity but also because bulk impurities have a strong tendency of surface segregation.[30,31] This problem can be circumvented by replacing bulk materials with thin films which can be grown epitaxially onto single-crystalline surfaces of refractory metals, such as Mo or W(110).[32] These REM films contain lower numbers of interstitial (C, N, and O) and substitutional (Fe and Pd) impurities.[33] By selecting appropriate growth parameters and subsequent annealing conditions, films with high surface quality can be prepared. For the work presented here, Dy films with thicknesses ranging from $\Theta=14$ AL to $\Theta=450$ AL were prepared by thermal evaporation onto a W(110) single crystal held at RT and subsequent annealing. Dy is evaporated from an electron-beam-heated W crucible at a rate of $r_{Dy}=9\pm1$ AL/min. Subsequently, the samples are annealed at temperatures between 490 and 680 K for 4 min. For a Dy coverage larger than 14 AL, this process results in continuous and flat Dy films.

As reported previously in Ref. 33, the comparison of the LEED patterns of clean and Dy-covered W(110) reveals a Nishiyama-Wassermann epitaxial relationship,[34–37] i.e., Dy(0001)$\|$W(110) and Dy[$0\bar{1}10$]$\|$W[$1\bar{1}0$]. Our AES data show a very low impurity level for the most common contaminants, such as O and C, and no W signal. The morphology of Dy/W(100) films is characterized by the presence of linear defects, i.e., screw dislocations with $\vec{b}=[0001]$ and misfit-induced edge dislocations with $\vec{b}=\langle 2\bar{1}\bar{1}0\rangle$. As we have shown recently, the dislocation density strongly depends on the film thickness and on details of the preparation procedure.[38] These defects play a crucial role in the magnetic structure of the films, especially in thin films where the magnetic domain structure is dominated by the interaction between misfit dislocations and domain walls.[38]

C. Surface electronic properties

Within the band gap of the (0001) surface-projected bulk, band structure of all trivalent lanthanides a $5d_{z^2}$-like surface state can be found at the $\bar{\Gamma}$ point. This d_{z^2}-like surface state has been observed by means of (inverse) photoelectron spectroscopy.[39] The surface state is characterized by a very flat band, i.e., low dispersion. It is strongly localized to the surface layer and can easily be detected by STS since the d_{z^2} orbital extends far into the vacuum.[18] In magnetic REM, due to the interaction with the localized $4f$ electrons, the surface state exhibits an exchange splitting that scales with the $4f$ magnetic moment.[40] This exchange splitting results in an occupied state below E_F with the spin parallel to the $4f$ spin (majority spin) and an unoccupied minority spin state.[18,41,42] At low temperature ($T=10$ K), the majority part of the Dy(0001) surface state appears at $E\simeq-100$ meV and the minority part at $E\simeq+400$ meV resulting in a spin splitting $\Delta_{ex}\simeq500$ meV.[40]

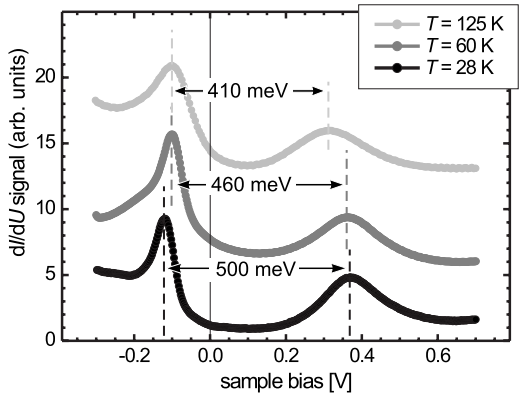

FIG. 2. dI/dU spectra of Dy(0001) taken with bare W tips at $T=28$ K, $T=60$ K, and $T=125$ K. The majority and minority parts of the $5d_{z^2}$-like surface state appear as narrow peaks below and above E_F, respectively. The exchange splitting decreases monotonously with increasing temperature.

IV. RESULTS

A. Structural and surface electronic properties

Figure 2 shows spin-averaged dI/dU spectra of the Dy(0001) surface taken with a clean W tip on 45 AL Dy on W(110) at $T=28$ K, $T=60$ K, and $T=125$ K, corresponding to 1/3, 3/4, and 3/2 of T_C, respectively. Irrespective of the actual measurement temperature, the characteristic double-peak structure typical for (0001)-terminated surfaces of the trivalent lanthanides can clearly be recognized. At low temperature, $T=28$ K, we find peak positions which are consistent with Ref. 40. Similar to previous temperature-dependent measurements on Tb(0001) and Gd(0001), the exchange splitting decreases with increasing temperature, mainly due to the displacement of the minority part of the surface state toward E_F.[43]

As shown in Fig. 3, the intensity of the dI/dU signal which is roughly proportional to the sample's local density of states varies only slightly if measured with a nonmagnetic tip. Figures 3(a) and 3(b) show STM topographs and enhanced contrast maps of the spin-averaged dI/dU signal at $U=-0.2$ V, respectively, of 90 AL Dy on W(110) taken with a clean tungsten tip. In contrast to the clean W(110) substrate which exhibits almost parallel and infinite steps edges (not shown), the morphology of the Dy film is dominated by differently oriented step edges of finite length. In each case, two of these steps merge at the point where a screw dislocation appears on the surface. A more detailed study of these dislocations and a model of their origin can be found in Ref. 38. The simultaneously measured dI/dU signal of the surface is almost homogeneous. In fact, a histogram of the dI/dU signal taken from the lower panel in (b) excluding step edges shows a rather narrow-peaked behavior with a relative width at half maximum of 4% only. Contrast enhancement reveals weak long-range modulations around the core of the screw

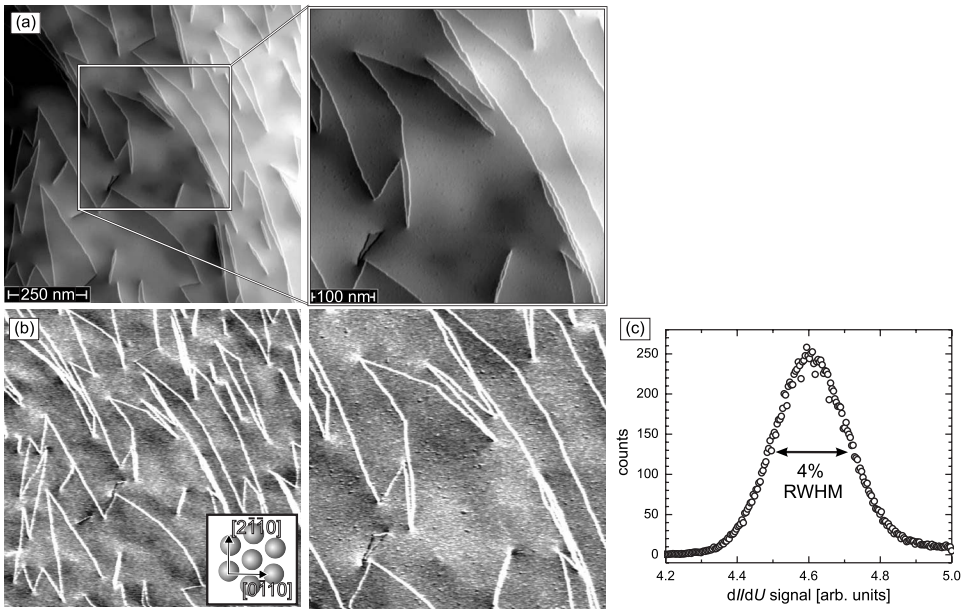

FIG. 3. (a) STM topographs and (b) spin-averaged dI/dU maps of 90 AL Dy on W(110) measured with a nonmagnetic W tip. Only a weak modulation of the dI/dU signal around the screw dislocations can be recognized. (c) Histogram of the dI/dU signal taken from the right panel in (b) (without step edges) shows a single peak with a relative width at half maximum of 4% only (tunneling parameters: $U=-0.2$ V, $I=15$ nA, and $T=60$ K).

dislocations [Fig. 3(b)]. We attribute this modulation to the stress field around the dislocation which decreases with the inverse of the distance to the dislocation core.[44] As we will show in the next chapter, experiments performed with magnetic tips lead to much stronger variations of the dI/dU signal.

B. Magnetic contrast studies

1. Domain mapping

In the following, we describe spin-resolved STM experiments which have been performed with Dy cluster tips. As we will point out below, we frequently obtained the strongest magnetic contrasts at relatively large negative bias voltages, i.e., far beyond the energetic position of the occupied part of the Dy surface state. For example, Figs. 4(a) and 4(b) show the topography and the dI/dU map of 90 AL Dy on W(110) measured with $U=-1.0$ V, respectively. While the dI/dU signal was essentially homogeneous if measured with a clean W tip (see Fig. 3), a characteristic pattern with discrete dI/dU levels can be recognized in Fig. 4(b). The histogram of this data set which is plotted in Fig. 4(c) reveals six well-separated peaks labeled i–vi from lowest to highest intensity of the dI/dU signal. The measured relative variation of the dI/dU signal is much larger than in experiments carried out with nonmagnetic tips [see Fig. 3(c)].

As schematically shown in the inset of Fig. 4(c), $\vec{m}_t$ is tilted by α with respect to domain vi which—since $0° < \alpha < 30°$ as described in Fig. 1(a)—leads to six different projections of $\vec{m}_s$ onto $\vec{m}_t$. Considering the sixfold symmetry of the Dy(0001) surface, it is a straightforward conclusion that $\vec{m}_s$ of domain i forms an angle of ±60° with domains ii and iii, ±120° with $\vec{m}_s$ of domains iv and v, and is opposed to $\vec{m}_s$ of domain vi. The experimentally determined values of the dI/dU signal intensity for the six domains are summarized in the second column of Table I. On the basis of Eq. (1), the magnetic dI/dU signal can be decomposed in a spin-averaged part, dI/dU_{SA}, and a spin-dependent part, dI/dU_{SP}. dI/dU_{SA} can be obtained by calculating the arithmetic average of the dI/dU values in Table I, resulting in $dI/dU_{SA}=1.22\pm0.03$ a.u. If the tip-sample distance were constant over all magnetic domains, i.e., in the case of vanishing polarization of the *total* tunneling current, the absolute value of dI/dU_{SP} for domains with opposite polarization, e.g., domains i and vi in Table I, should be equal. In our case, however, the total tunneling current was spin polarized resulting in a slight magnetization-dependent variation of the tip-sample distance. This effect introduces a small error in the calculation of α. Based on Eq. (1), we can solve the following equation for the dI/dU signal of each domain $n=\mathrm{i},\ldots,\mathrm{vi}$;

$$dI/dU_n = dI/dU_{SA} + dI/dU_{SP_n} = dI/dU_{SA} + dI/dU_{SP_{coll}}\cos(\alpha+\theta_n), \quad (2)$$

by using a variational approach. Here, $dI/dU_{SP_{coll}}$ is the spin-polarized contribution in the case of collinear tip and sample magnetization and $\theta_n = 0°, -60°, +60°, -120°, +120°, 180°$ for $n=1,\ldots,6$, respectively. For this particular case, we obtain $\alpha=(8\pm4)°$. This result is drawn schematically in the inset of Fig. 4(c) where $\vec{m}_t$ and $\vec{m}_s$ are indicated by the arrows.

As pointed out in Sec. II B above, $\vec{m}_t$ and $\vec{m}_s$ of the domain with the largest dI/dU signal may accidentally assume angles of $\alpha=30°$ or $\alpha=0°$ leading to three or four contrast levels, respectively [see Figs. 1(b) and 1(c)]. For example, Figs. 4(d) and 4(e) show the topography and the dI/dU map of 135 AL Dy on W(110), respectively. The histogram of Fig. 4(e) which is plotted in (f) reveals three contrast levels only.

2. Tunneling spectra

As pointed out in the preceding section, we frequently obtained the strongest magnetic contrasts at relatively large negative bias voltages. In order to understand the origin of this observation, we have measured tunneling spectra within

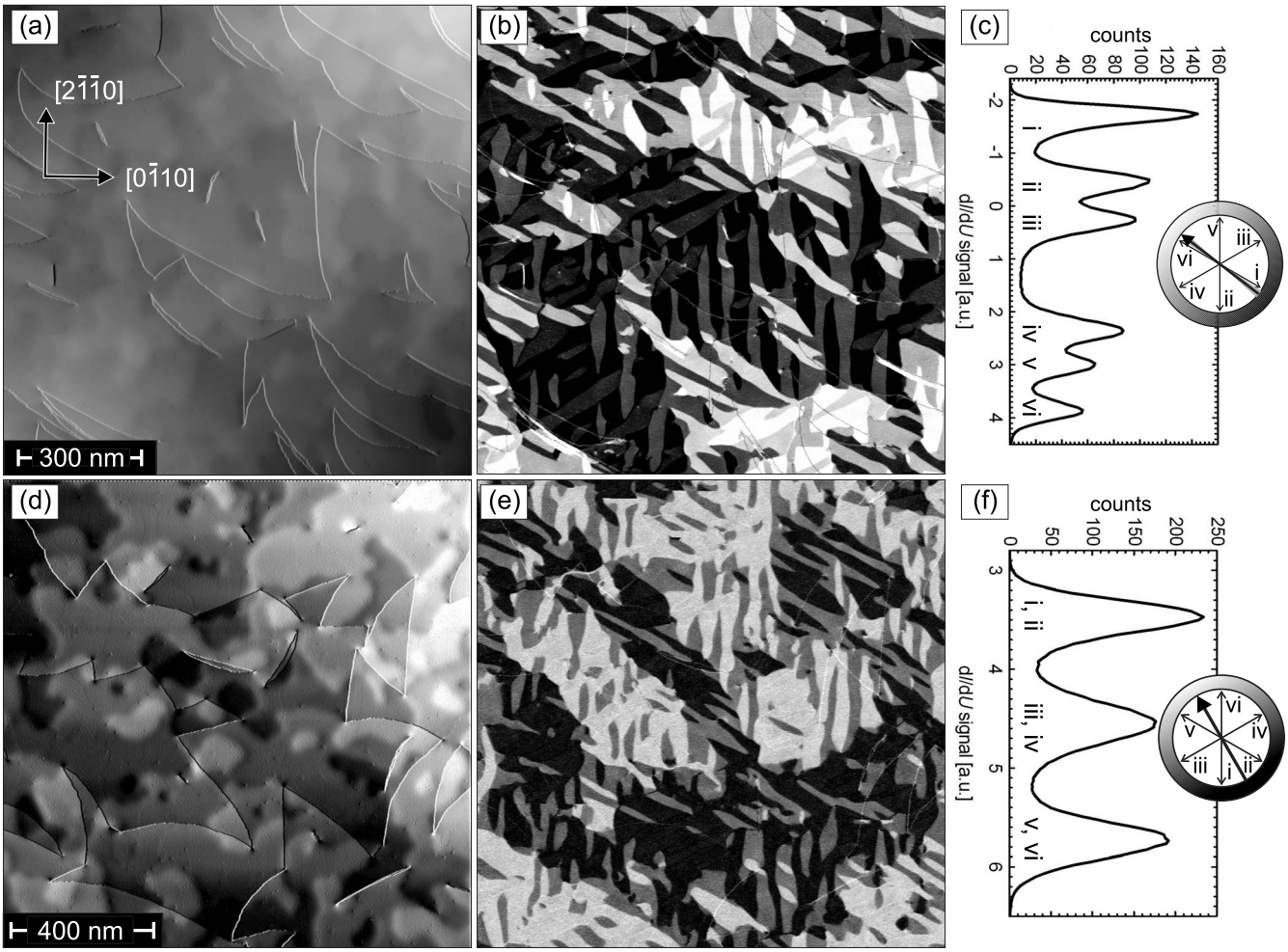

FIG. 4. (a) Topography and (b) spin-resolved dI/dU map of a 90 AL Dy/W(110) film ($T=25$ K, $U=-1.0$ V, and $I=30$ nA). (c) The histogram of the dI/dU map shown in (b) reveals six contrast levels. (d) Topography and (e) spin-resolved dI/dU map of a 90 AL Dy/W(110) film ($T=60$ K, $U=-0.2$ V, and $I=15$ nA). (f) The histogram of this dI/dU map shows only three contrast levels.

a large bias range (-2 V$\leqslant$U$\leqslant+0.8$ V) using different nonmagnetic and magnetically coated tips. Figure 5(a) shows a typical spectrum of the Dy(0001) surface taken with a nonmagnetic W tip. This spectrum is dominated by the occupied and empty parts of the surface state at $U\simeq-0.1$ V and $U\simeq+0.4$ V, respectively. Note that there is only a small feature around $U=-0.75$ V. At high negative sample bias, a monotonously increasing dI/dU signal is observed. Figures 5(b) and 5(c) show spectra taken with different Dy cluster tips. Now, both sets of spectra are dominated by a strongly polarized peak around $U=-0.8$ V. This structure is typical for spectra taken with Dy cluster tips, although the actual position of the "main" peak slightly varies between $U=-0.9$ V and $U=-0.7$ V. Asymmetries as high as $A=50\%$ at the main peak position were frequently measured. We can exclude that this peak is caused by an electronic state of the Dy(0001) sample since earlier angle-resolved photoemission spectroscopy data reveal that the Dy(0001) surface exhibits no characteristic electronic features around -0.8 eV below the Fermi level.[45] The occupied state which is closest to the Fermi level is a Δ_2 bulk band at a binding energy $E_b\approx1.5$ eV. Obviously, this feature is not observed in the STS spectra of Fig. 5(c). Probably, the Δ_2 bulk band rapidly decays into the vacuum resulting in a vanishing density of states at the tip position. Since the dI/dU peaks around $U=-0.8$ V cannot be correlated to sample states, we assign them to highly spin-polarized unoccupied states of the small Dy cluster at the tip apex. In fact, it is well known that STS spectra are dominated by tip states at negative bias voltage.[46]

TABLE I. Analysis of the intensity of the dI/dU signal in Fig. 4(b).

Domain index	$\frac{dI}{dU}$ (expt.) (a.u.)	$\frac{dI}{dU_{SP}}$ (calc.) (a.u.)
i	−1.74±0.02	−2.96±0.05
ii	−0.449±0.013	−1.66±0.04
iii	0.262±0.012	−0.95±0.04
iv	2.36±0.02	1.14±0.05
v	2.99±0.02	1.77±0.05
vi	3.88±0.02	2.66±0.05

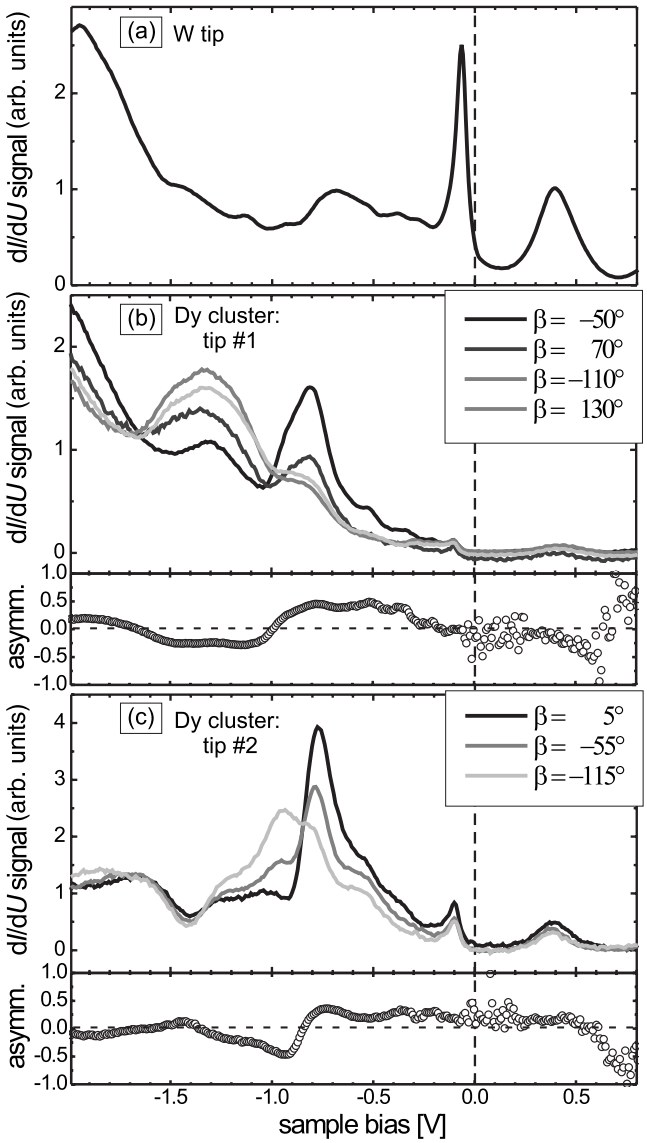

FIG. 5. Tunneling spectra of 90 AL Dy/W(110) films measured with different tips (T=52 K and U_{stab}=−2 V). β indicates the angle between $\vec{m}_s$ and $\vec{m}_t$. (a) STS data taken with a bare W tip (I_{stab} =45 nA). (b) SP-STS data (top panel) taken with a Dy cluster tip on four domains with different $\vec{m}_s$ and asymmetry (bottom) between the spectra from β=−50° and β=130° (I_{stab}=45 nA). (c) SP-STS spectra (top) with a Dy cluster tip on three domains with different $\vec{m}_s$ and asymmetry (bottom) between the spectra from β=5° and β=−115° .

C. Domain structure of Dy(0001)/W(110)

In an earlier publication, we have shown that the magnetic domain structure of Dy thin films on W(110) is closely linked to the morphology.[38] In particular, an effective pinning of the domain walls by screw and edge dislocations was found by correlating growth studies, atomic resolution STM, and spin-resolved domain images. The results revealed that for films thicker than 60 AL, the defect density continuously decreases. Since the domain wall energy increases with increasing film thickness while the potential energy associated with subsurface defects remains essentially constant, pinning becomes less and less important as very thick Dy films are considered.

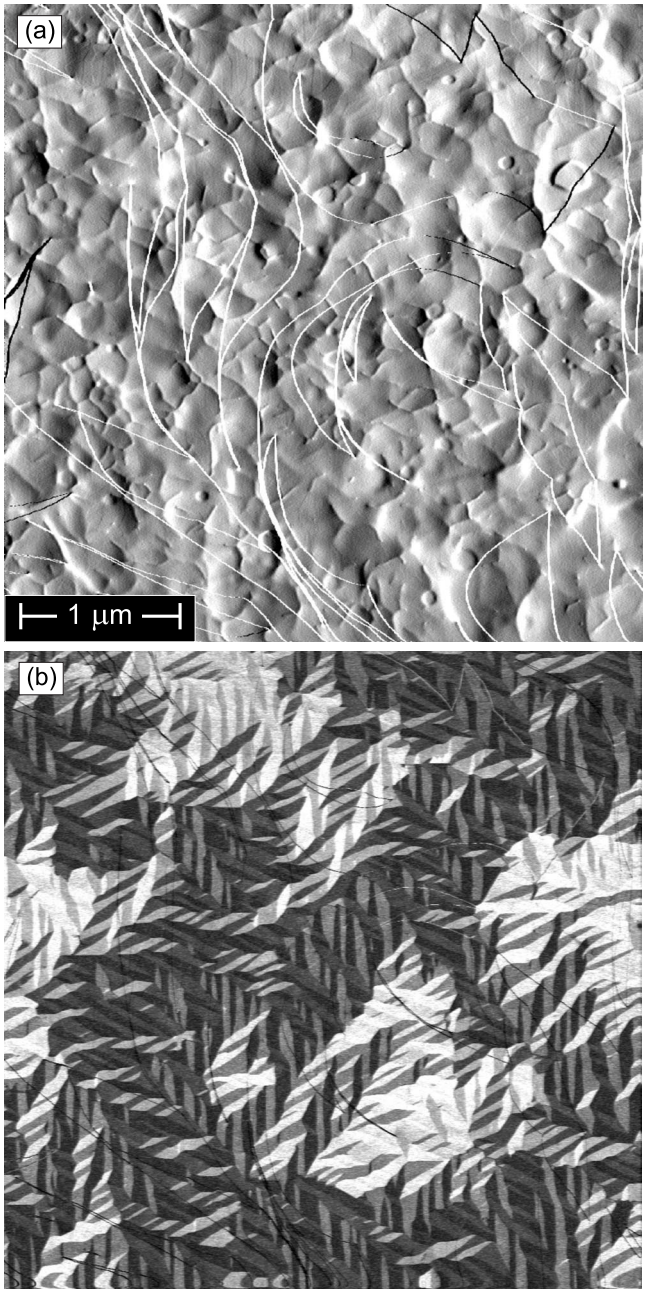

FIG. 6. (a) Differentiated STM topograph and (b) magnetic dI/dU map of a 4×4 μm^2 area of 450 AL Dy/W(110) film (T =60 K, and U=−0.6 V, and I=30 nA).

Figure 6(a) shows the topography and the magnetic structure of a 4×4 μm^2 area of a 450 AL Dy/W(110) film. The bumpy film topography is caused by the existence of subsurface gliding planes with $\vec{b}=\pm\frac{1}{2}[0001]$. Already in early stages of the growth, they lead to the relaxation of differently stacked patches and were overgrown subsequently.[38] As can be seen in the simultaneously measured magnetic dI/dU map of Fig. 6(b), the magnetic structure is characterized by a stripe domain pattern with two types of domains, the magnetization direction of which alternate by 60°. These struc-

tures are as long as 800 nm. The width of these stripe domains amounts to about 40 nm and is very regular. Probably, the large magnetoelastic coupling in Dy results in a rather limited and regular domain size.

The well-ordered domain structure of thick Dy/W(110) films allows for a detailed study of $\vec{m}_s$. As mentioned before, adjacent domains are mostly separated by 60° domain walls. For a domain with a specific $\vec{m}_s$, only two 60° domain walls are possible, namely, with a ±60° rotation of $\vec{m}_s$ to the adjacent domain. These two possible 60° domain walls run along close-packed directions, as can be seen in Fig. 4(b). As an example, domain i is mainly surrounded by patches of domains ii and iii. The magnetic charge σ_s at an interface between two regions with magnetizations $\vec{m}_1$ and $\vec{m}_2$ can be calculated as

$$\sigma_s = \vec{n} \cdot (\vec{m}_1 - \vec{m}_2), \tag{3}$$

where $\vec{n}$ is the interface normal. It is well known that domain walls with zero magnetic charges are energetically favorable. In this framework, the condition for the formation of an energy-free magnetic interface (page 119 in Ref. 47) is

$$\vec{n} \cdot (\vec{m}_1 - \vec{m}_2) = 0. \tag{4}$$

Therefore, domain walls in Dy(0001) which separate patches of domains i and ii are always oriented along the same crystallographic direction, $[2\bar{1}\bar{1}0]$, while domain walls separating patches of domains i and iii run along $[1\bar{2}10]$.

This relation may be used to determine $\vec{m}_s$ of the entire sample. For example, Fig. 7 shows the magnetization directions of 90 AL Dy on W(110). It shall be noted, however, that without an external field available, we cannot determine the absolute direction of $\vec{m}_s$; two mirror-symmetric solutions are always possible. A detailed analysis of the domain walls in Fig. 7 reveals the presence of a few 120° domain walls, three of which are marked by black ellipses, and one 180° domain wall (white ellipse). The spin structure of the different domain walls and the dependence of the domain wall width on the rotation angle will be analyzed in the following paragraphs.

D. Domain walls

Figure 8 presents a study of the internal spin structure of domain walls observed on 90 AL Dy/W(110). Figure 8(a) shows the domain structure of 90 AL Dy on W(110). A histogram of the dI/dU signal intensity of Fig. 8(a) is shown in Fig. 8(b). Figures 8(c)–8(f) show line profiles of the magnetic dI/dU signal across two different 60° domain walls, a 120° domain wall, and a 180° domain wall labeled (c)–(f) in Fig. 8(a), respectively. The horizontal lines in the domain wall profiles [(c)–(f)] represent the peak positions in the histogram of Fig. 8(b). While the dI/dU signal changes monotonously for the two 60° domain walls, an extremal dI/dU value, i.e., a nonmonotonous profile, is observed in the cases of the 120° domain wall and the 180° domain wall.

In the following, we have compared the experimentally observed 180° domain wall profile with model calculations. Two classes of 180° domain walls are considered: Bloch domain walls [see Fig. 9(a)] where $\vec{m}_s$ rotates around the domain wall normal, i.e., into the out-of-plane directions in the wall center, and Néel domain walls [see Fig. 9(b)] where $\vec{m}_s$ rotates around a vector within the domain wall such that the magnetization remains within the film plane. For the qualitative conclusions we will draw in the following, it is sufficient to assume the simple tanh-shaped profile of the magnetization angle as it is known from domain walls in uniaxial systems (for further information of the model, see Ref. 47, Chap. 3.6.1). ϕ and α are the polar and azimuthal angles of $\vec{m}_t$ with respect to the surface normal and $\vec{m}_s$ of the domain with the highest dI/dU signal, respectively. Since we know

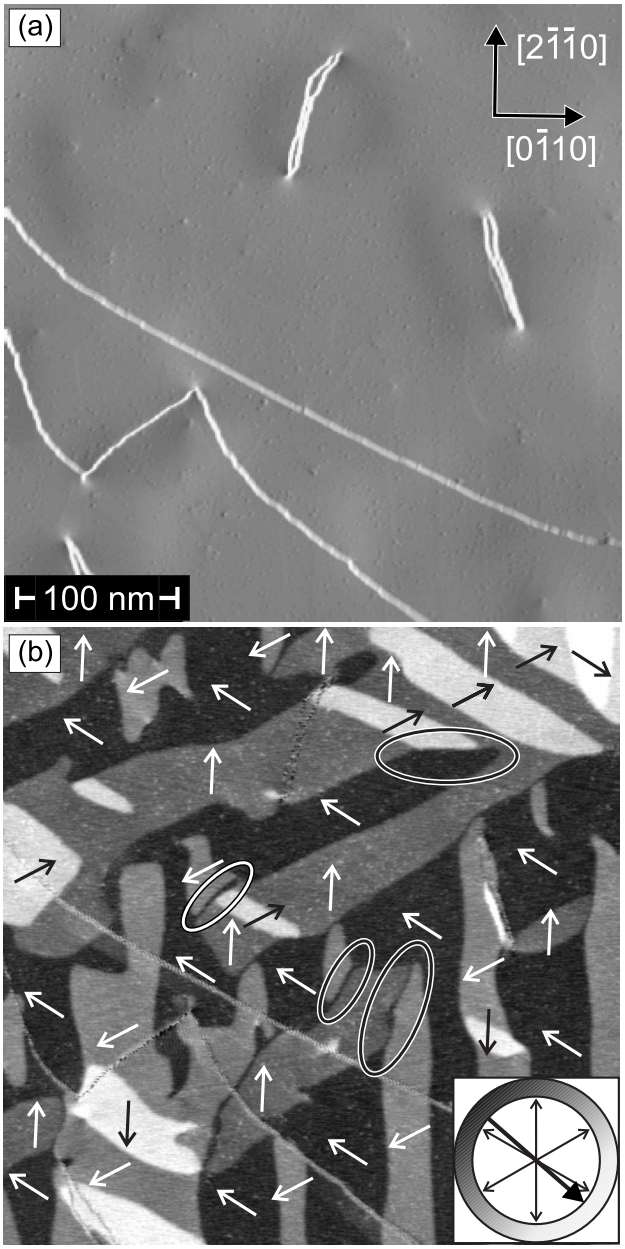

FIG. 7. (a) STM topograph and (b) magnetic dI/dU map of a 90 AL Dy/W(110) film (T=25 K, U=−1.0 V, and I=21 nA). The arrows indicate the sample's local magnetization directions $\vec{m}_s$ with easy axes along $\langle 2\bar{1}\bar{1}0 \rangle$.

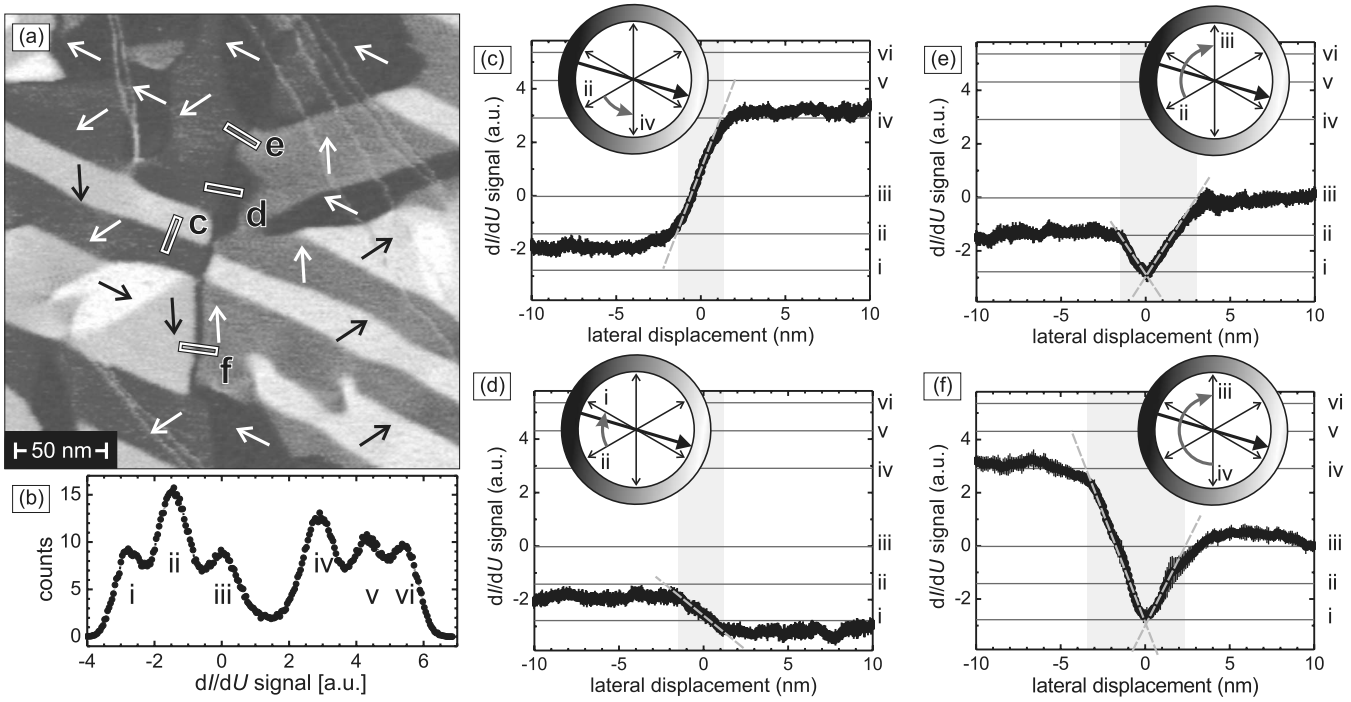

FIG. 8. Domain wall profile analysis of a 90 AL Dy/W(110) film. (a) Spin-resolved dI/dU map of 90 AL Dy/W(110) showing the magnetic domain structure (T=59 K, U=−0.6 V, and I=30 nA). (b) The histogram of the data shown in (a) reveals six peaks. The directions of $\vec{m}_s$ for the domains is indicated in (a) by arrows. (c)–(f) Line profiles and schematic representation of the path of the magnetization for the domain walls labeled with (c)–(f) in (a). The profiles of the two 60° domain walls shown in (c) and (d) reveal a domain wall width of about 2.5 nm.

that the magnetization of our Dy cluster tips is almost perfectly in plane, we can choose ϕ=0. Under these boundary conditions, Bloch domain walls—irrespective of the actual value of α—always maintain their general shape but only the amplitude varies [lower panel of Fig. 9(a)]. In contrast, as shown in the lower panel of Fig. 9(b), the shape of Néel walls depends on α. While a point-or mirror-symmetric domain wall profile is obtained for α=0° and α=90°, respectively, the profile becomes asymmetric for $0° < \beta < 90°$.

Comparison of the experimental 180° domain profile in Fig. 8(f) with the calculated domain profiles in Fig. 9 reveals that the domain walls at the Dy/W(110) surface are Néel

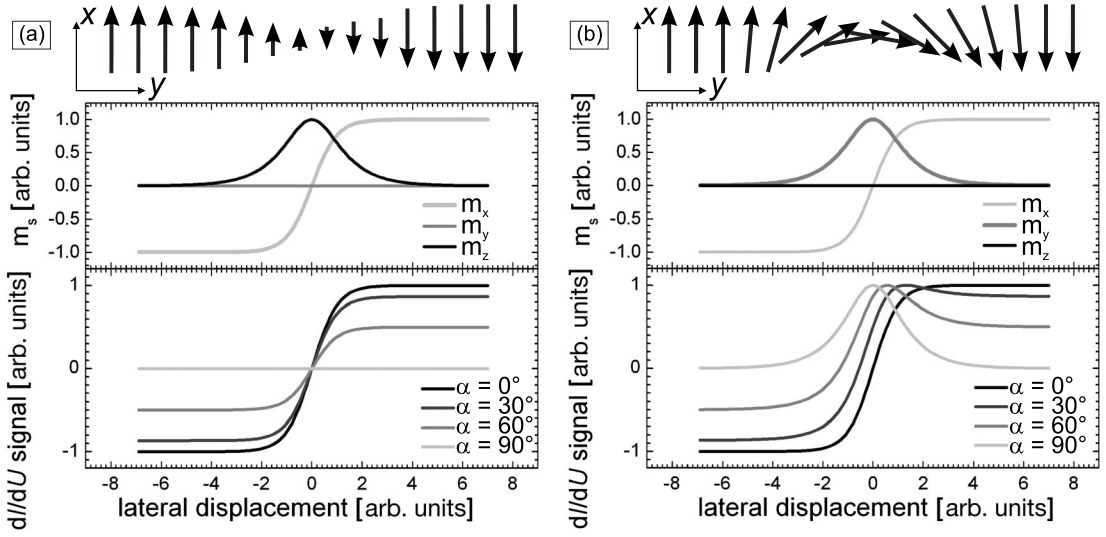

FIG. 9. Model of 180° domain wall profiles taken with an in-plane sensitive tip where $\vec{m}_t$ forms an angle α with the x direction. (a) Model of the $\vec{m}_s$ projected onto the surface x-y plane (top panel) for a Bloch domain wall with a simple profile, $\vec{m}_s$ projection (middle), and the magnetic dI/dU profile (bottom) on the basis of Eq. (1). (b) Model of the $\vec{m}_s$ projected onto the surface x-y plane (top panel) for a Néel domain wall with a simple profile, $\vec{m}_s$ projection (middle), and the magnetic dI/dU profile (bottom).

walls. This result is in contrast to the behavior of ferromagnetic bulk materials which prefer Bloch domain walls because this avoids internal magnetic charges.[47] Furthermore, the large uniaxial anisotropy along the c axis of bulk Dy (Refs. 48–50) should also result in the formation of Bloch domain walls. We have to consider, however, that the surface magnetic anisotropy differs from the bulk and that the magnetization distribution of Bloch walls produces a magnetic stray field, too. Therefore, the Bloch walls of a ferromagnetic sample are usually capped with a Néel-type structure.[51,52] In fact, experiments with Cr-coated tips which typically give out-of-plane sensitivity did not provide any indication for an out-of-plane component of the surface magnetization. Since the 120° and 180° domain wall profiles in Figs. 8(e) and 8(f) exhibit only one point of inflection, we may conclude that the magnetoelastic energy dominates over the magnetocrystalline anisotropy energy at the surface (page 228 in Ref. 47), as expected from the large magnetostriction of bulk Dy.[53,54] Otherwise, large-angle domain walls would decompose into several successive 60° domain walls.

Néel domain walls may exhibit two possible paths for the magnetization inside the domain wall, clockwise and anticlockwise. For 60° and 120° domain walls, the magnetization will always run along the shortest path since this minimizes the total energy. In the case of 180° domain walls, however, both rotational senses are energetically degenerate. The path of the magnetization inside the domain walls is schematically represented in the insets in Figs. 8(c)–8(f). While Eq. (4) dictates that 120° domain walls always run along $\langle 0\bar{1}10\rangle$ directions, no preferential orientation is obtained for 180° domain walls. The observed domain wall widths amount to 25 and 4.5 nm for 60° and 120° domain walls.

It is well known that Néel domain walls consist of three parts, a core with tails on either side. Within the core, the magnetization direction changes on a lateral scale given by the effective exchange length $\sqrt{A/(K_u+K_d)}$, where A is the exchange stiffness constant and K_u and K_d are the uniaxial magnetocrystalline and dipolar magnetic anisotropy energy density, respectively. According to Ref. 47, the tail width is determined by $w_{\mathrm{tail}} \approx \exp -\gamma D K_d/K_u$, with Euler's constant $\gamma \approx 0.577$ and the film thickness D. Since K_d is much larger than K_u, soft materials exhibit a sharply localized core and a very wide tail. Rare-earth metals, in contrast, possess a large magnetocrystalline anisotropy and the magnetoelastic coupling is very strong. This may result in a Néel tail width which is comparable to the core width. While the tails are not visible for the 60° and 120° domain walls shown in Figs. 8(c)–8(e), it may be recognized by kinks in the dI/dU signal in Fig. 8(f) showing the 180° domain wall. Our analysis gives a core width of about 5 nm and tails which are approximately 3 nm wide. This value is in reasonable agreement with theoretical studies of domain walls in rare earths performed by Egami and Graham.[55] They calculated the spin structure of 180° domain walls in basal (0001) planes of ferromagnetic bulk dysprosium, i.e., perpendicular to the domain wall orientation in our experiments. Their calculation considers the exchange interaction up to the fourth nearest neighbor and only the K_2 and K_6^6 anisotropy constants for the anisotropy energy. A very sharp domain wall with a thickness of $t \simeq 2$ nm was obtained. We speculate that the interaction of the tails may be responsible for the regularly arranged domain and domain wall structure observed in Fig. 6.

V. SUMMARY

In summary, we have imaged the domain and domain wall structure of thin Dy films which were epitaxially grown on W(110). Our spin-polarized STM studies clearly reveal that the surface of Dy films is ferromagnetically ordered for thicknesses larger than 14 AL. No evidence of the near-surface helimagnetic phase could be observed. A sixfold symmetry of the surface results in domains which are mainly separated by 60° domain walls. These domains alternate with a periodicity of about 40 nm. An analysis of domain wall profiles reveals that the surface is dominated by Néel walls and the width of the tail is comparable to the core width. The domain wall width amounts to 2.5, 4.5, and 5 nm for 60°, 120°, and 180° domain walls, respectively.

ACKNOWLEDGMENTS

Financial support from DFG Project No. BO 1468/17-1 and the EU project "ASPRINT" is gratefully acknowledged.

*Corresponding author; present address: Lawrence Berkeley National Laboratory, Berkeley, CA 94720; ljberbil-bautista@lbl.gov
†Present address: Center for Nanoscale Materials, Argonne National Laboratory, Argonne, IL 60439.

[1] R. J. Elliott, Phys. Rev. **124**, 346 (1961).
[2] R. E. Watson, A. J. Freeman, and J. P. Dimmock, Phys. Rev. **167**, 497 (1968).
[3] B. Johansson, L. Nordström, O. Eriksson, and M. S. S. Brooks, Phys. Scr., T **T39**, 100 (1991).
[4] A. S. Chernyshov, A. O. Tsokol, A. M. Tishin, K. A. Gschneidner, and V. K. Pecharsky, Phys. Rev. B **71**, 184410 (2005).
[5] C. F. Majkrzak, J. Kwo, M. Hong, Y. Yafet, D. Gibbs, C. L. Chien, and J. Bohr, Adv. Phys. **40**, 99 (1991).
[6] M. Ciria, J. I. Arnaudas, A. del Moral, G. J. Tomka, C. de la Fuente, P. A. J. de Groot, M. R. Wells, and R. C. C. Ward, Phys. Rev. Lett. **75**, 1634 (1995).
[7] K. Dumesnil, C. Dufour, P. Mangin, G. Marchal, and M. Hennion, Phys. Rev. B **54**, 6407 (1996).
[8] K. Dumesnil, A. Stunault, P. Mangin, C. Vettier, D. Wermeille, N. Bernhoeft, S. Langridge, C. Dufour, and G. Marchal, Phys. Rev. B **58**, 3172 (1998).
[9] V. Leiner, M. Ay, and H. Zabel, Phys. Rev. B **70**, 104429 (2004).
[10] E. Weschke *et al.*, Phys. Rev. Lett. **93**, 157204 (2004).
[11] H. Ott, C. Schüßler-Langeheine, E. Schierle, G. Kaindl, and E. Weschke, Appl. Phys. Lett. **88**, 212507 (2006).

[12] J. B. Kortright, D. D. Awschalom, J. Stohr, S. D. Bader, Y. U. Idzerda, S. P. P. Parkin, I. K. Schuller, and H. C. Siegmann, J. Magn. Magn. Mater. **207**, 7 (1999).
[13] R. Wiesendanger, Microsc. Res. Tech. **66**, 59 (2005).
[14] M. Bode, Rep. Prog. Phys. **66**, 523 (2003).
[15] M. Bode, E. Y. Vedmedenko, K. von Bergmann, A. Kubetzka, P. Ferriani, S. Heinze, and R. Wiesendanger, Nat. Mater. **5**, 477 (2006).
[16] R. Meservey and P. M. Tedrow, Phys. Rep. **238**, 173 (1994).
[17] E. Y. Tsymbal, O. N. Mryasov, and P. LeClair, J. Phys.: Condens. Matter **15**, R109 (2003).
[18] M. Bode, M. Getzlaff, and R. Wiesendanger, Phys. Rev. Lett. **81**, 4256 (1998).
[19] W. Wulfhekel and J. Kirschner, Appl. Phys. Lett. **75**, 1944 (1999).
[20] U. Schlickum, W. Wulfhekel, and J. Kirschner, Appl. Phys. Lett. **83**, 2016 (2003).
[21] M. Bode, O. Pietzsch, A. Kubetzka, and R. Wiesendanger, J. Electron Spectrosc. Relat. Phenom. **114-116**, 1055 (2001).
[22] A. Kubetzka, M. Bode, O. Pietzsch, and R. Wiesendanger, Phys. Rev. Lett. **88**, 057201 (2002).
[23] T. K. Yamada, M. M. J. Bischoff, T. Mizoguchi, and H. van Kempen, Appl. Phys. Lett. **82**, 1437 (2003).
[24] A. Wachowiak, J. Wiebe, M. Bode, O. Pietzsch, M. Morgenstern, and R. Wiesendanger, Science **298**, 577 (2002).
[25] D. Wortmann, S. Heinze, P. Kurz, G. Bihlmayer, and S. Blügel, Phys. Rev. Lett. **86**, 4132 (2001).
[26] J. Tersoff and D. R. Hamann, Phys. Rev. Lett. **50**, 1998 (1983).
[27] J. Tersoff and D. R. Hamann, Phys. Rev. B **31**, 805 (1985).
[28] D. R. Behrendt, S. Legvold, and F. H. Spedding, Phys. Rev. **109**, 1544 (1958).
[29] M. K. Wilkindon, W. C. Koehler, E. O. Wollan, and J. W. Cable, J. Appl. Phys. **32**, 48S (1961).
[30] S. C. Wu, H. Li, Y. S. Li, D. Tian, J. Quinn, F. Jona, and D. Fort, Phys. Rev. B **44**, 13720 (1991).
[31] J. Quinn, Y. S. Li, F. Jona, and D. Fort, Phys. Rev. B **46**, 9694 (1992).
[32] J. Kołaczkiewicz and E. Bauer, Surf. Sci. **175**, 487 (1986).
[33] H. Li, D. Tian, J. Quinn, Y. S. Li, S. C. Wu, and F. Jona, Phys. Rev. B **45**, 3853 (1992).
[34] J. H. van der Merwe, Philos. Mag. A **45**, 127 (1982).
[35] J. H. van der Merwe, Philos. Mag. A **45**, 145 (1982).
[36] J. H. van der Merwe, Philos. Mag. A **45**, 159 (1982).
[37] J. H. van der Merwe, Appl. Surf. Sci. **22/23**, 545 (1985).
[38] S. Krause, L. Berbil-Bautista, T. Hänke, F. Vonau, M. Bode, and R. Wiesendanger, Europhys. Lett. **76**, 637 (2006).
[39] E. Weschke, C. Schüssler-Langeheine, R. Meier, A. V. Fedorov, K. Starke, F. Hübinger, and G. Kaindl, Phys. Rev. Lett. **77**, 3415 (1996).
[40] D. Wegner, A. Bauer, A. Rehbein, and G. Kaindl, Jpn. J. Appl. Phys., Part 1 **45**, 1941 (2006).
[41] D. Li, J. Pearson, S. D. Bader, D. N. McIlroy, C. Waldfried, and P. A. Dowben, Phys. Rev. B **51**, 13895 (1995).
[42] M. Donath, B. Gubanka, and F. Passek, Phys. Rev. Lett. **77**, 5138 (1996).
[43] M. Bode, M. Getzlaff, A. Kubetzka, R. Pascal, O. Pietzsch, and R. Wiesendanger, Phys. Rev. Lett. **83**, 3017 (1999).
[44] H. G. V. Bueren, *Imperfections in Crystals* (North-Holland, Amsterdam, 1960).
[45] C. Schüßler-Langeheine, Ph.D. thesis, Freie Universität Berlin, 1999.
[46] V. A. Ukraintsev, Phys. Rev. B **53**, 11176 (1996).
[47] A. Hubert and R. Schäfer, *Magnetic Domains* (Springer, New York, 1998).
[48] E. Callen and H. B. Callen, J. Phys. Chem. Solids **27**, 1271 (1966).
[49] J. J. Rhyne and A. E. Clark, J. Appl. Phys. **38**, 1379 (1967).
[50] J. L. Feron, Ph.D. thesis, University of Grenoble, 1969.
[51] H. P. Oepen and J. Kirschner, Phys. Rev. Lett. **62**, 819 (1989).
[52] M. R. Scheinfein, J. Unguris, R. J. Celotta, and D. T. Pierce, Phys. Rev. Lett. **63**, 668 (1989).
[53] S. Legvold, J. Alstad, and J. Rhyne, Phys. Rev. Lett. **10**, 509 (1963).
[54] F. J. Darnell, Phys. Rev. **132**, 128 (1963).
[55] T. Egami and C. D. Graham, J. Appl. Phys. **42**, 1299 (1971).